

# Raman Microscopy and Associated Techniques for Label-Free Imaging of Cancer Tissue



**Title:**

Raman microscopy and associated techniques for label-free imaging of cancer tissue

**Running title (35 chars including spaces):**

Raman microscopy of cancer tissue

**Author:**

Andrew Downes

**Affiliation:**

Institute for Bioengineering, University of Edinburgh, United Kingdom.

**Abstract**

Raman spectroscopy can identify cancerous from healthy tissue, with a chemical analysis from the measurement of vibrational bond frequencies. However, to detect small tumours a form of Raman imaging is required. Such imaging – by acquiring a Raman spectrum at each imaging pixel - can detect tumours, but is rather slow. Multi-photon versions of Raman – anti-Stokes Raman scattering (CARS) microscopy and stimulated Raman scattering (SRS) microscopy – offer similar accuracies in identifying cancerous tissue and tumor margins, but with a far higher speed which is beneficial for diagnosis of small tumors in tissue. SRS microscopy can also be used to image extrinsic molecules in living cells, such as anti-cancer drugs at typical concentrations.

**Introduction to Raman techniques**

Raman scattering of light by vibrational bonds in molecules and crystals (1) results in a photon losing a well-defined amount of energy in exciting the vibration. This is shown in the energy level diagram in Fig. 1. An alternative explanation is that measured frequency shifts of laser light after interacting with a sample, are equal to the frequencies of vibration of the bonds within that sample. Spectroscopy of the frequency-shifted light reveals many different vibrational modes present in a sample, and therefore is a measure of its chemistry. It is extremely well suited to characterizing living cells and tissues, as visible or near-infrared light can be focussed to produce very small focal volumes for intracellular measurement, and also high resolution images. It is minimally invasive at moderate laser powers, and does not require labels such as fluorophores or nanoparticles, so is appropriate for long term studies of living cells, and the diagnosis of disease in humans.

However, for biological tissues the efficiency is low – only the order of 1 in $10^{10}$ photons is Raman-shifted (2). This low efficiency is due to the excitation of a low frequency vibration with high frequency light. A good quality spectrum takes 1-100 secs to acquire, depending on laser wavelength and power. A Raman image can be produced by sequentially acquiring a Raman spectrum at each imaging pixel, but this is typically too slow for live cell imaging. Such a Raman spectrometer capable of confocal imaging (3) is depicted in Fig 2(a). By using a far higher power laser and distributing this power along a line at the sample by using a cylindrical lens, a line-scanning Raman system (4, 5) is able to acquire several spectra in parallel – from all the positions along the line focussed on the sample. This speeds us the Raman image acquisition time enough to enable live cell imaging.

Coherent anti-Stokes Raman scattering (CARS) microscopy (6) uses two different laser frequencies to excite a molecular vibration much more efficiently. In order for 3 photons to interact in CARS, short laser pulses need to be applied. These pulse durations should ideally be matched to the vibrational lifetimes of molecular vibrations – typically 1 - 20 ps (7). Traditional 'narrowband' CARS uses picosecond lasers with well-defined frequencies, so that only one vibrational mode is excited within an image. This gives typically 5-6 orders of magnitude increase in signal levels (8) – hence imaging speeds can be as fast as video rate, but the downside is that only one vibrational mode is imaged. In order to provide more robust chemical imaging, more than one vibrational mode can be imaged sequentially by retuning one laser frequency between images, in what can be termed multi-spectral CARS (9). A schematic of a narrowband CARS microscope is shown in Fig 2(b). CARS also has the disadvantage of producing a signal which is proportional to the square of the concentration (hence low concentrations cannot be probed), and is combined with a constant background signal. These problems can be addressed in several ways (10-13), normally at the expense of imaging speed.

Multiplex (or, hyperspectral) CARS (14) has one narrowband (picosecond) laser with sub-nanometer linewidth, and one broadband laser with tens or hundreds of nanometers linewidth, in order to excite a wide range of vibrational frequencies. This can either cover a relatively small range of the Raman spectrum, or the majority of the Raman spectrum of biomolecules. As the laser power of the broadband pulse is dispersed over a wide range of vibrational modes, and the resulting signal is split into a large number of channels on the CCD detector, it is significantly slower than narrowband CARS. It has the advantage of acquiring a spectrum or partial spectrum at each imaging pixel, rather than just the intensity of one peak within the spectrum. At down to 3.5ms per spectrum (15) - i.e. per pixel - its speed is comparable with line-scanning Raman systems.

Stimulated Raman scattering (SRS) (16) offers speeds similar to narrowband CARS – as fast as video rate – with a linear dependence of the signal on concentration. In SRS two photons are absorbed more readily than single photons, so when the low energy (Stokes) beam is switched off, the amount of the high energy (pump) beam transmitted through the sample increases. Full modulation of the Stokes beam produces a modulation of $<10^{-4}$ of the pump beam, which is measured with a lock-in amplifier (16). However, it cannot easily be extended to hyperspectral imaging.

**Raman spectroscopy of cancer tissues**

Raman spectroscopy was first applied to cancer tissue in 1996 (17), with principal component analysis (PCA) used for a quantitative assignment (as healthy or cancerous) in 1998 (18). Another statistical method, partial least squares was used to assign a chemical composition to cancerous tissue in 2005 (19), from a known database of constituants. As spectroscopy is not the main thrust of this review, the reader is directed towards a review of Raman spectroscopy for cancer diagnosis (20). Most Raman spectroscopy cancer diagnosis is performed on *ex vivo* tissue, but has also been extended to blood serum (21). The combined use of Raman spectroscopy with metal nanoparticles, termed surface-enhanced Raman spectroscopy (SERS) is reviewed here (22).

Raman spectroscopy has been applied *in vivo* (23) with the use of an endoscopic probe (22). A review of *in vivo* Raman spectroscopy is presented here (24), and of *in vivo* cancer diagnosis here (25).

An example set of Raman spectra are shown in Fig 3, from primary and secondary tumors in head and neck lymph nodes, and benign tissue for comparison (26). There is a high degree of similarity between spectra from all three types of tissue, which is to be expected given the relatively small differences between their biochemistries. In order to extract these small differences from the acquired spectra, and ignore the similarities, some statistical analysis is required.

Each Raman spectrum can be decomposed into a set of basis spectra, with a measured spectrum processed into a linear composition of the basis set spectra. Several statistical methods exist, notable principal component analysis (PCA) (27), partial least squares (28), linear discriminant analysis (29), and ant colony analysis (30). For diagnosis of an unknown tissue (e.g. as healthy or cancerous), all techniques require a 'training set' of spectra from known tissue types (e.g. healthy and cancerous), and convert the complexity of a spectrum into the simplicity of a single data point normally in a two-dimensional plot. An example is presented in Fig. 3, for spectra acquired on known primary tumors, secondary tumors, and benign tissue (26). Then, when an unknown sample is measured, its spectrum is inserted into the model and plotted with the training set – hence giving an assignment of what tissue type the spectrum most closely resembles. The accuracy of Raman measurements in cancer diagnosis is typically in the range 85-95%. Partial least squares analysis (31, 32) is also able to decompose spectra into a known spectral library of components (e.g. DNA, collagen, phospholipids).

Although Raman spectroscopy offers a highly accurate measure of whether a small region of tissue is cancerous or not, by acquiring a single spectrum we cannot hope to find the extent of a tumor within healthy tissue. An averaged Raman spectrum over a large area of tissue would miss small tumors, as the spectrum would seem to be mostly healthy tissue. Spectroscopy cannot hope to identify tumor margins within tissue, so some type of imaging is required. Such a form of imaging based on Raman

spectroscopy would be extremely useful in producing a label-free version of the current standard for tissue biopsy imaging – haematoxylin and eosin (H&E) staining, shown later in Fig 5b.

**Raman imaging of cancer tissues**

Confocal Raman imaging often uses spectral acquisition times of the order of 1 second at each imaging pixel to produce a hyperspectral image. Such a long pixel dwell time would be too slow for imaging of living cells, so to achieve sub-100 msec pixel dwell times a high power green laser is required (33). It has been reported that live cell confocal Raman imaging cannot be repeated for more than a handful of images, as cumulative photodamage occurs. Reducing the laser intensity by transforming focal spot into a line and acquiring line-scanning Raman images, would most likely not improve the acquisition rate because photodamage is cumulative and originates from photochemical reactions rather than any change in temperature.

Some data analysis needs to be performed, as a spectrum cannot be displayed at each image pixel. Each Raman spectrum can be compared with a Raman spectra from other pixels within the image, to produce similar regions - this process is called cluster analysis (34) . Alternatively, spectra can be decomposed into a combination of spectra of suspected components from a library of spectra with partial least squares analysis, yielding quantitative images of the concentrations of these components. This was applied to a breast duct within healthy tissue, to produce images of the concentration of collagen, cell cytoplasm, and cell nucleus (35). In a similar way, the concentration of a drug within a cancer cell can be measured and imaged (36-38).

Confocal Raman images have also been successfully classified into organelles within a cancer cell (nucleus, mitochondria, endoplasmic reticulum, Golgi apparatus, and cytoskeleton) (33). These images, displayed in Fig. 4, offer a label-free alternative to fluorescent dyes.

The Lodz group (39-41) acquired confocal Raman images of cancerous and non-cancerous breast tissue, distinguishing them by their different biochemistries present in the Raman spectra. The best separation in images was given by the amount of carotenoids at 1518 $cm^{-1}$, but also observed changes in protein and lipid content.

Kong et al. (42) applied confocal Raman imaging to skin cancer, which is shown in Fig. 5. Converting the set of spectra into an image was achieved by k-means cluster analysis which separated images into regions which were assigned as basal cell carcinoma (BCC), muscle, fat, dermis, inflamed dermis, epidermis, substrate, and unknown. Comparison with stained tissue sections was good, but some areas identified as BCC were false positives.

Although high resolution confocal Raman imaging has its uses in imaging cancer cells and tissue, its application to diagnosis of cancer tissue and cells is limited: a diffraction-limited spot is too small a sample volume to assign each pixel as cancerous or healthy. There is also a problem with scale: at 5-20 hours per $mm^2$ (42), it is far too slow for practical implementation as a replacement for haematoxylin & eosin staining. The Nottingham group (43) have used segmentation of autofluorescence or white light images of tissue to determine what are likely to be similar regions, then acquire one spectrum from each region. This is almost as effective as normal confocal Raman but speeds up image acquisition by a factor of ~100, so is applicable to samples of a few $mm^2$.

**High speed Raman imaging of cancer tissues**

Confocal Raman imaging can be performed with a pixel dwell time of <50 msec using a high power laser, and line scanning Raman imaging with an acquisition time of 1 s per line (36). However, this acquisition time corresponds to several hours for an image with sufficient pixels required for cancer diagnosis of tissue. In order to improve potential throughput, CARS microscopy (either acquiring the intensity of one peak within the spectrum with narrowband CARS, or a full spectrum with multiplex CARS) has been applied to imaging of cancer cells and tissue.

Narrowband CARS microscopy has been applied to cancer cells in a number of ways. Firstly, the technique is ideally suited to imaging of lipids, as lipids produce a strong signal at the C-$H_2$ stretch frequency of 2845 $cm^{-1}$, especially when concentrated into droplets in the cytoplasm. The Purdue group (44) demonstrated that lipid-rich environments promote metastasis, and were able to identify circulating tumor cells *in vivo* with CARS by their lipid content.

Secondly, deuterated molecules can be introduced and tracked with narrowband CARS, as the stretch frequency of the C-$D_2$ bond is shifted to 2150 $cm^{-1}$. At this frequency there are no naturally occurring vibrational bonds in cells, so image contrast and detectability are highest. This was applied to measurement of lipid uptake in cancer cells (44), to monitor metabolism and kinetics. Although not strictly a label-free technique, deuterium substitution for hydrogen only has minor effects on the kinetics of molecules, whereas tagging with a fluorescent dye could dramatically affect the behaviour of molecules of interest – such as whether it is able to cross the cell membrane.

Thirdly, by acquiring multiple images and rapidly retuning the frequency between each frame, a set of images can be acquired which have essentially the same information as hyperspectral imaging. Instead of acquiring a spectrum at each pixel position, a series of images at each vibrational frequency are acquired. This multi-spectral imaging has been applied to imaging of organelles in cancer cells (45), by acquiring images in the range 2800 - 3100 $cm^{-1}$. Each pixel is assigned as either nucleus, nucleolus, endoplasmic reticulum, lipid droplet, Golgi apparatus, or mitochondria, by comparing the 'spectrum' of values using a supervised learning algorithm. Using this method, cellular imaging is free from the requirement of staining cells to reveal the presence of organelles. Results are similar to the acquisition of a full Raman spectrum at each pixel, which were shown in Fig. 4.

SRS microscopy has been used on living cancer cells to also image organelles (46), by acquiring 80 images in the frequency range 2840 – 3070 $cm^{-1}$, with a total acquisition time of 3-4 minutes. Multivariate techniques were used to produce images of components (lipids, DMSO, and protein / nucleotide).

SRS microscopy is well suited to imaging of external molecules, such as deuterated lipids and drugs, or amino acids (47). The SRS signal is linear in concentration, whereas CARS imaging produces signals which are quadratically dependent on concentration. Thus lower concentration limits can be probed with SRS. Molecules of interest can be 'tagged' with deuterium, or by modifying the molecule to contain a single alkyne bond which has a frequency of 2125 $cm^{-1}$. Alkyne imaging (48) has reached a concentration level of 200 μM for a pixel dwell time of 100 μsec (49). This is demonstrated in Fig. 6, where an alkyne-tagged thymidine analog, 5-ethynyl-2'-deoxyuridine (EdU) is imaged in living cancer cells, where its presence is determined to be entirely within the nucleus.

Narrowband CARS microscopy has been applied to cancer tissue. The Edinburgh group imaged paraffin-embedded breast cancer tissue sections, which were dewaxed to remove the paraffin – as well as other lipids. They acquired images (50) at a frequency of 1660 $cm^{-1}$ (whose vibrations are dominated by proteins like those in Fig. 6), along with SHG of collagen. This label-free imaging showed a high degree of similarity with a haematoxylin & eosin stained section. Later the group refined this method to CARS imaging at 2930 $cm^{-1}$ (51), which is the dominant Raman peak for proteins (52) and has been shown to be the dominant peak in Raman spectroscopy of cancerous tissue (53). When the group combined this CARS image with a TPEF image of autofluorescent elastin, and an SHG image of collagen, a 3-color label-free image in Fig. 7 is produced which displays significantly more information than the corresponding stained tissue.

This multi-modal microscopy, comprising CARS, TPEF, and SHG, has also successfully been applied to skin cancer (54), but with a CARS frequency of 2850 $cm^{-1}$ relating to the $CH_2$ stretch. CARS can also be used to image cellular morphology. By tuning the frequency to 2845 $cm^{-1}$, the cytoplasm is clearly visible as bright, with the nucleus appearing darker. Simply by comparing cell size and shape with known values for healthy and cancerous frozen lung tissue, an accuracy of diagnosis of over 90% was achieved (55). Brain tumors were identified by a reduction in the lipid content (56) with narrowband CARS imaging at the $CH_2$ frequency (2850 $cm^{-1}$).

By combining $CH_2$ and $CH_3$ imaging at 2850 $cm^{-1}$ and 2930 $cm^{-1}$, brain tumors and tumor margins were clearly identified in SRS microscopy (57) with extremely good contrast and high specificity, over large areas. The technique was also applied in vivo, with the results shown in Fig. 8. Neuropathologists were used to give a correlation between SRS imaging and haematoxylin & eosin (H&E) staining, of $\kappa = 0.98$.

Multiplex CARS (mCARS) microscopy could potentially offer superior contrast to narrowband CARS or SRS as it acquires a full or partial Raman spectrum at each pixel, albeit at the expense of imaging speed. In one publication, cancerous and non-cancerous cell lines are distinguished by mCARS imaging (58). When mCARS was applied to healthy brain tissue, spectra at each imaging pixel were classified as myelin, grey matter, granule cells and Purkinje cells using PCA (59), resulting in 4 separate images of these classifications.

The most significant application of mCARS microscopy was in being able to differentiate cancer versus normal fresh tissue sections (53) with an accuracy above 99% and define cancer boundaries to +-100 µm, again with an accuracy of more than 99%. Images of 63 x 63 pixels were acquired in less than 5 minutes. The spectral differences were dominated by a higher $CH_2$ peak at 2845 $cm^{-1}$ for healthy tissue, and a higher $CH_3$ peak at 2930 $cm^{-1}$ for cancerous tissue, agreeing with the narrowband CARS results shown in Fig. 7.

**Conclusions**

Raman spectroscopy offers a high degree of accuracy when comparing healthy and cancerous tissue, so why do we need to perform Raman imaging? For pathology of tissue biopsies, sample sizes will be several millimetres or even centimeters in diameter. So tumors which are small relative to the size of the biopsy would be missed either by picking a spot at random, or by averaging the spectrum over a large area. Indeed, most Raman spectroscopy studies either use a large focal spot or average over a

large area (0.1 – 1 mm in diameter) which is already clearly cancerous when viewed in the H&E stained image.

Although confocal Raman microscopy may offer an improved accuracy over haematoxylin & eosin (H&E) staining, it would be a relatively slow replacement. Instead, a higher speed variant would be preferable – either line-scanning Raman microscopy or multiplex CARS offer reasonable imaging speeds of minutes per image, with the benefit of acquiring a full spectrum. However, it seems that for cancer diagnosis the main differences between healthy and cancerous tissue can be reduced to the $CH_3$ and $CH_2$ peaks within the spectrum. In this case, far higher speed can be achieved with narrowband CARS microscopy, or with SRS microscopy. When combined with SHG of collagen, and TPEF of elastin or cells, a multi-modal microscopy should enhance Raman-based chemical information with other signals which alter between healthy and cancerous tissue. This information could be either presented as a false color image to a pathologist, or combined into a quantitative value, of probability that the tissue is cancerous. One further benefit of high speed multi-modal imaging is that it can be acquired on fresh tissue, so 3D image stacks can be acquired.

*In vivo* imaging is hard to achieve at imaging depths more than a few millimeters using optical techniques. For this reason, *in vivo* cancer imaging will be greatly limited in humans, to skin cancers or where endoscopy can be performed. Even so, there are significant technical issues with performing multi-photon endoscopy.

**References**


1. Raman CV, Krishnan KS. A new type of secondary radiation. Nature. 1928;121(3048):501-2.
2. Hokr BH, Bixler JN, Noojin GD, Thomas RJ, Rockwell BA, Yakovlev VV, et al. Single-shot stand-off chemical identification of powders using random Raman lasing. Proceedings of the National Academy of Sciences. 2014;111(34):12320-4. doi: 10.1073/pnas.1412535111.
3. Williams KPJ, Pitt GD, Batchelder DN, Kip BJ. Confocal Raman Microspectroscopy Using a Stigmatic Spectrograph and CCD Detector. Applied Spectroscopy. 1994;48(2):232-5 UR - http://as.osa.org/abstract.cfm?URI=as-48-2-.
4. Hamada K, Fujita K, Smith NI, Kobayashi M, Inouye Y, Kawata S. Raman microscopy for dynamic molecular imaging of living cells. Journal of Biomedical Optics. 2008;13(4):044027--4. doi: 10.1117/1.2952192.
5. Harada Y, Ota T, Ping D, Yamaoka Y, Hamada K, Fujita K, et al., editors. Imaging of anticancer agent distribution by a slit-scanning Raman microscope2008.
6. Zumbusch A, Holtom GR, Xie XS. Three-dimensional vibrational imaging by coherent anti-Stokes Raman scattering. Physical Review Letters. 1999;82(20):4142-5.
7. Laubereau A, von der Linde D, Kaiser W. Direct Measurement of the Vibrational Lifetimes of Molecules in Liquids. Physical Review Letters. 1972;28(18):1162-5.
8. Kachynski AV, Kuzmin AN, Prasad PN, Smalyukh II. Realignment-enhanced coherent anti-Stokes Raman scattering and three-dimensional imaging in anisotropic fluids. Opt Express. 2008;16(14):10617-32 KW - Anisotropic optical materials KW - Liquid crystals KW - Three-dimensional microscopy KW - Nonlinear optics, four-wave mixing KW - Spectroscopy, coherent anti-Stokes Raman scattering UR - http://www.opticsexpress.org/abstract.cfm?URI=oe-16-14-. doi: 10.1364/OE.16.010617.
9. Garbacik ET, Korai RP, Frater EH, Korterik JP, Otto C, Offerhaus HL. In planta imaging of Δ9-tetrahydrocannabinolic acid in Cannabis sativa L. with hyperspectral coherent anti-Stokes Raman scattering microscopy. Journal of Biomedical Optics. 2013;18(4):046009-. doi: 10.1117/1.JBO.18.4.046009.
10. Cheng JX, Book LD, Xie XS. Polarization coherent anti-Stokes Raman scattering microscopy. Opt Lett. 2001;26(17):1341-3. doi: 10.1364/ol.26.001341. PubMed PMID: 18049602.
11. Jurna M, Korterik JP, Otto C, Herek L, Offerhaus HL, editors. Background free CARS imaging by local phase detection2009.
12. Konorov SO, Blades MW, Turner RFB. Non-resonant background suppression by destructive interference in coherent anti-Stokes Raman scattering spectroscopy. Opt Express. 2011;19(27):25925-34 KW - Coherent optical effects KW - Multiphoton processes KW - Nonlinear optics, four-wave mixing KW - Spectroscopy, multiphoton KW - Spectroscopy, Raman UR - http://www.opticsexpress.org/abstract.cfm?URI=oe-19-27-. doi: 10.1364/OE.19.025925.
13. Ganikhanov F, Evans CL, Saar BG, Xie XS. High-sensitivity vibrational imaging with frequency modulation coherent anti-Stokes Raman scattering (FM CARS) microscopy. Opt Lett. 2006;31(12):1872-4 KW - Microscopy KW - Scanning microscopy KW - Nonlinear optics, four-wave mixing KW - Spectroscopy, coherent anti-Stokes Raman scattering UR - http://ol.osa.org/abstract.cfm?URI=ol-31-12-. doi: 10.1364/OL.31.001872.
14. Müller M, Schins JM. Imaging the Thermodynamic State of Lipid Membranes with Multiplex CARS Microscopy. The Journal of Physical Chemistry B. 2002;106(14):3715-23. doi: 10.1021/jp014012y.
15. Camp JrCharles H, Lee YJ, Heddleston JM, Hartshorn CM, WalkerAngela RH, Rich JN, et al. High-speed coherent Raman fingerprint imaging of biological tissues. Nat Photon. 2014;8(8):627-34. doi: 10.1038/nphoton.2014.145


http://www.nature.com/nphoton/journal/v8/n8/abs/nphoton.2014.145.html#supplementary-information.

16. Freudiger CW, Min W, Saar BG, Lu S, Holtom GR, He C, et al. Label-Free Biomedical Imaging with High Sensitivity by Stimulated Raman Scattering Microscopy. Science. 2008;322(5909):1857-61. doi: 10.1126/science.1165758.
17. Mahadevan-Jansen A, Richards-Kortum RR. Raman spectroscopy for the detection of cancers and precancers. Journal of Biomedical Optics. 1996;1(1):31-70. doi: 10.1117/12.227815.
18. Mahadevan-Jansen A, Mitchell MF, Ramanujamf N, Malpica A, Thomsen S, Utzinger U, et al. Near-Infrared Raman Spectroscopy for In Vitro Detection of Cervical Precancers. Photochemistry and Photobiology. 1998;68(1):123-32. doi: 10.1111/j.1751-1097.1998.tb03262.x.
19. Haka AS, Shafer-Peltier KE, Fitzmaurice M, Crowe J, Dasari RR, Feld MS. Diagnosing breast cancer by using Raman spectroscopy. Proceedings of the National Academy of Sciences of the United States of America. 2005;102(35):12371-6. doi: 10.1073/pnas.0501390102.
20. Fenn MB, Xanthopoulos P, Pyrgiotakis G, Grobmyer SR, Pardalos PM, Hench LL. Raman spectroscopy for clinical oncology. Advances in Optical Technologies. 2011;2011.
21. González-Solís J, Martínez-Espinosa J, Torres-González L, Aguilar-Lemarroy A, Jave-Suárez L, Palomares-Anda P. Cervical cancer detection based on serum sample Raman spectroscopy. Lasers Med Sci. 2014;29(3):979-85. doi: 10.1007/s10103-013-1447-6.
22. Vendrell M, Maiti KK, Dhaliwal K, Chang Y-T. Surface-enhanced Raman scattering in cancer detection and imaging. Trends in Biotechnology. 2013;31(4):249-57. doi: http://dx.doi.org/10.1016/j.tibtech.2013.01.013.
23. Wang W, Zhao J, Short M, Zeng H. Real-time in vivo cancer diagnosis using raman spectroscopy. Journal of Biophotonics. 2014;9999.
24. Matousek P, Stone N. Recent advances in the development of Raman spectroscopy for deep non-invasive medical diagnosis. Journal of Biophotonics. 2013;6(1):7-19. doi: 10.1002/jbio.201200141.
25. Wang W, Zhao J, Short M, Zeng H. Real-time in vivo cancer diagnosis using raman spectroscopy. Journal of Biophotonics. 2014;9999(9999):n/a-n/a. doi: 10.1002/jbio.201400026.
26. Lloyd GR, Orr LE, Christie-Brown J, McCarthy K, Rose S, Thomas M, et al. Discrimination between benign, primary and secondary malignancies in lymph nodes from the head and neck utilising Raman spectroscopy and multivariate analysis. Analyst. 2013;138(14):3900-8. doi: 10.1039/C2AN36579K.
27. Sharaf MA. Chemometrics: John Wiley & Sons; 1986.
28. Geladi P, Kowalski BR. Partial least-squares regression: a tutorial. Analytica Chimica Acta. 1986;185(0):1-17. doi: http://dx.doi.org/10.1016/0003-2670(86)80028-9.
29. Fisher RA. THE USE OF MULTIPLE MEASUREMENTS IN TAXONOMIC PROBLEMS. Annals of Eugenics. 1936;7(2):179-88. doi: 10.1111/j.1469-1809.1936.tb02137.x.
30. Allegrini F, Olivieri AC. A new and efficient variable selection algorithm based on ant colony optimization. Applications to near infrared spectroscopy/partial least-squares analysis. Analytica Chimica Acta. 2011;699(1):18-25. doi: http://dx.doi.org/10.1016/j.aca.2011.04.061.
31. Haaland DM, Timlin JA, Sinclair MB, Van Benthem MH, Martinez MJ, Aragon AD, et al., editors. Multivariate curve resolution for hyperspectral image analysis: applications to microarray technology. Biomedical Optics 2003; 2003: International Society for Optics and Photonics.
32. Ljungqvist MG, Ersboll B, Kobayashi K-i, Nakauchi S, Frosch S, Nielsen ME, editors. Near-infrared hyper-spectral image analysis of astaxanthin concentration in fish feed coating. Imaging systems and techniques (IST), 2012 IEEE International Conference on; 2012: IEEE.
33. Klein K, Gigler Alexander M, Aschenbrenner T, Monetti R, Bunk W, Jamitzky F, et al. Label-Free Live-Cell Imaging with Confocal Raman Microscopy. Biophysical Journal. 2012;102(2):360-8. doi: http://dx.doi.org/10.1016/j.bpj.2011.12.027.
34. Theiler J, Gisler G, editors. A contiguity-enhanced k-means clustering algorithm for unsupervised multispectral image segmentation. Proc SPIE; 1997.

35. Shafer-Peltier KE, Haka AS, Fitzmaurice M, Crowe J, Myles J, Dasari RR, et al. Raman microspectroscopic model of human breast tissue: implications for breast cancer diagnosis in vivo. Journal of Raman Spectroscopy. 2002;33(7):552-63.
36. Harada Y, Dai P, Yamaoka Y, Ogawa M, Tanaka H, Nosaka K, et al. Intracellular dynamics of topoisomerase I inhibitor, CPT-11, by slit-scanning confocal Raman microscopy. Histochem Cell Biol. 2009;132(1):39-46. doi: 10.1007/s00418-009-0594-0.
37. Salehi H, Derely L, Vegh A-G, Durand J-C, Gergely C, Larroque C, et al. Label-free detection of anticancer drug paclitaxel in living cells by confocal Raman microscopy. Applied Physics Letters. 2013;102(11):113701. doi: doi:http://dx.doi.org/10.1063/1.4794871.
38. El-Mashtoly SF, Petersen D, Yosef HK, Mosig A, Reinacher-Schick A, Kötting C, et al. Label-free imaging of drug distribution and metabolism in colon cancer cells by Raman microscopy. Analyst. 2014;139(5):1155-61.
39. Surmacki J, Musial J, Kordek R, Abramczyk H. Raman imaging at biological interfaces: applications in breast cancer diagnosis. Molecular cancer. 2013;12(1):48.
40. Abramczyk H, Brozek-Pluska B, Surmacki J, Jablonska-Gajewicz J, Kordek R. Raman 'optical biopsy' of human breast cancer. Progress in Biophysics and Molecular Biology. 2012;108(1–2):74-81. doi: http://dx.doi.org/10.1016/j.pbiomolbio.2011.10.004.
41. Brozek-Pluska B, Musial J, Kordek R, Bailo E, Dieing T, Abramczyk H. Raman spectroscopy and imaging: applications in human breast cancer diagnosis. Analyst. 2012;137(16):3773-80.
42. Kong K, Rowlands CJ, Varma S, Perkins W, Leach IH, Koloydenko AA, et al. Diagnosis of tumors during tissue-conserving surgery with integrated autofluorescence and Raman scattering microscopy. Proceedings of the National Academy of Sciences. 2013;110(38):15189-94. doi: 10.1073/pnas.1311289110.
43. Takamori S, Kong K, Varma S, Leach I, Williams HC, Notingher I. Optimization of multimodal spectral imaging for assessment of resection margins during Mohs micrographic surgery for basal cell carcinoma. Biomed Opt Express. 2015;6(1):98-111 KW - Medical optics and biotechnology KW - Dermatology KW - Optical diagnostics for medicine KW - Raman spectroscopy UR - http://www.osapublishing.org/boe/abstract.cfm?URI=boe-6-1-98. doi: 10.1364/BOE.6.000098.
44. Le TT, Huff TB, Cheng J-X. Coherent anti-Stokes Raman scattering imaging of lipids in cancer metastasis. BMC cancer. 2009;9(1):42.
45. El-Mashtoly Samir F, Niedieker D, Petersen D, Krauss Sascha D, Freier E, Maghnouj A, et al. Automated Identification of Subcellular Organelles by Coherent Anti-Stokes Raman Scattering. Biophysical Journal. 2014;106(9):1910-20. doi: http://dx.doi.org/10.1016/j.bpj.2014.03.025.
46. Zhang D, Wang P, Slipchenko MN, Ben-Amotz D, Weiner AM, Cheng J-X. Quantitative vibrational imaging by hyperspectral stimulated Raman scattering microscopy and multivariate curve resolution analysis. Analytical chemistry. 2012;85(1):98-106.
47. Wei L, Yu Y, Shen Y, Wang MC, Min W. Vibrational imaging of newly synthesized proteins in live cells by stimulated Raman scattering microscopy. Proceedings of the National Academy of Sciences. 2013;110(28):11226-31.
48. Yamakoshi H, Dodo K, Palonpon A, Ando J, Fujita K, Kawata S, et al. Alkyne-Tag Raman Imaging for Visualization of Mobile Small Molecules in Live Cells. Journal of the American Chemical Society. 2012;134(51):20681-9. doi: 10.1021/ja308529n.
49. Wei L, Hu F, Shen Y, Chen Z, Yu Y, Lin C-C, et al. Live-cell imaging of alkyne-tagged small biomolecules by stimulated Raman scattering. Nat Meth. 2014;11(4):410-2. doi: 10.1038/nmeth.2878

http://www.nature.com/nmeth/journal/v11/n4/abs/nmeth.2878.html#supplementary-information.
50. Mouras R, Rischitor G, Downes A, Salter D, Elfick A. Nonlinear optical microscopy for drug delivery monitoring and cancer tissue imaging. Journal of Raman Spectroscopy. 2010;41(8):848-52. doi: 10.1002/jrs.2622.
51. Mouras R, Bagnaninchi P, Downes A, Elfick A. Multimodal, label-free nonlinear optical imaging for applications in biology and biomedical science. Journal of Raman Spectroscopy. 2013;44(10):1373-8. doi: 10.1002/jrs.4305.

52. Leikin S, Parsegian VA, Yang W-H, Walrafen GE. Raman spectral evidence for hydration forces between collagen triple helices. Proceedings of the National Academy of Sciences. 1997;94(21):11312-7.
53. Chowdary PD, Jiang Z, Chaney EJ, Benalcazar WA, Marks DL, Gruebele M, et al. Molecular histopathology by spectrally reconstructed nonlinear interferometric vibrational imaging. Cancer research. 2010;70(23):9562-9.
54. Heuke S, Vogler N, Meyer T, Akimov D, Kluschke F, Röwert-Huber H-J, et al., editors. Detection and Discrimination of Non-Melanoma Skin Cancer by Multimodal Imaging. Healthcare; 2013: Multidisciplinary Digital Publishing Institute.
55. Gao L, Li F, Thrall MJ, Yang Y, Xing J, Hammoudi AA, et al. On-the-spot lung cancer differential diagnosis by label-free, molecular vibrational imaging and knowledge-based classification. Journal of Biomedical Optics. 2011;16(9):096004--10. doi: 10.1117/1.3619294.
56. Uckermann O, Galli R, Tamosaityte S, Leipnitz E, Geiger KD, Schackert G, et al. Label-free delineation of brain tumors by coherent anti-stokes Raman scattering microscopy in an orthotopic mouse model and human glioblastoma. PloS one. 2014;9(9):e107115.
57. Ji M, Orringer DA, Freudiger CW, Ramkissoon S, Liu X, Lau D, et al. Rapid, Label-Free Detection of Brain Tumors with Stimulated Raman Scattering Microscopy. Science Translational Medicine. 2013;5(201):201ra119. doi: 10.1126/scitranslmed.3005954.
58. Jang Hyuk L, Eun Hee C, Sang-Mo S, Myoung-kyu O, Do-Kyeong K. Comparative Study of Breast Normal and Cancer Cells Using Coherent Anti-Stokes Raman Scattering Microspectroscopy Imaging. Applied Physics Express. 2012;5(8):082401.
59. Pohling C, Buckup T, Pagenstecher A, Motzkus M. Chemoselective imaging of mouse brain tissue via multiplex CARS microscopy. Biomed Opt Express. 2011;2(8):2110-6.

**Figures**

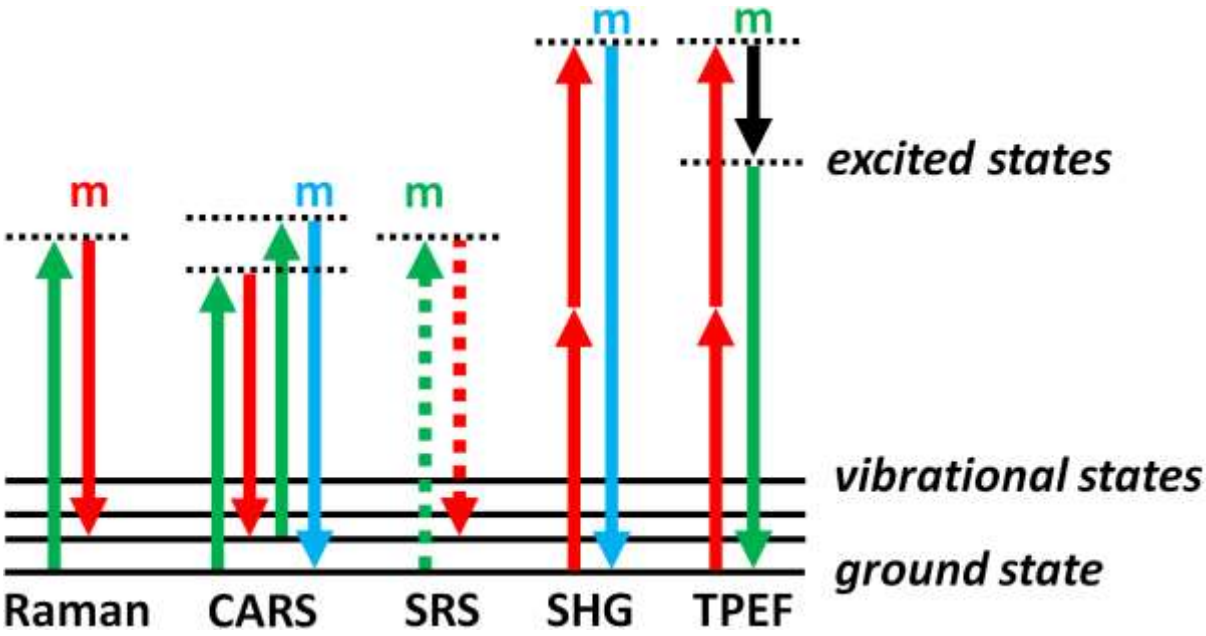


*Fig. 1. Energy level diagram for Raman scattering, coherent anti-Stokes Raman scattering (CARS), stimulated Raman scattering (SRS), second harmonic generation (SHG), and two-photon excitation fluorescence (TPEF). The letter 'm' refers to the photon which is measured, all other photons being required for illumination.*

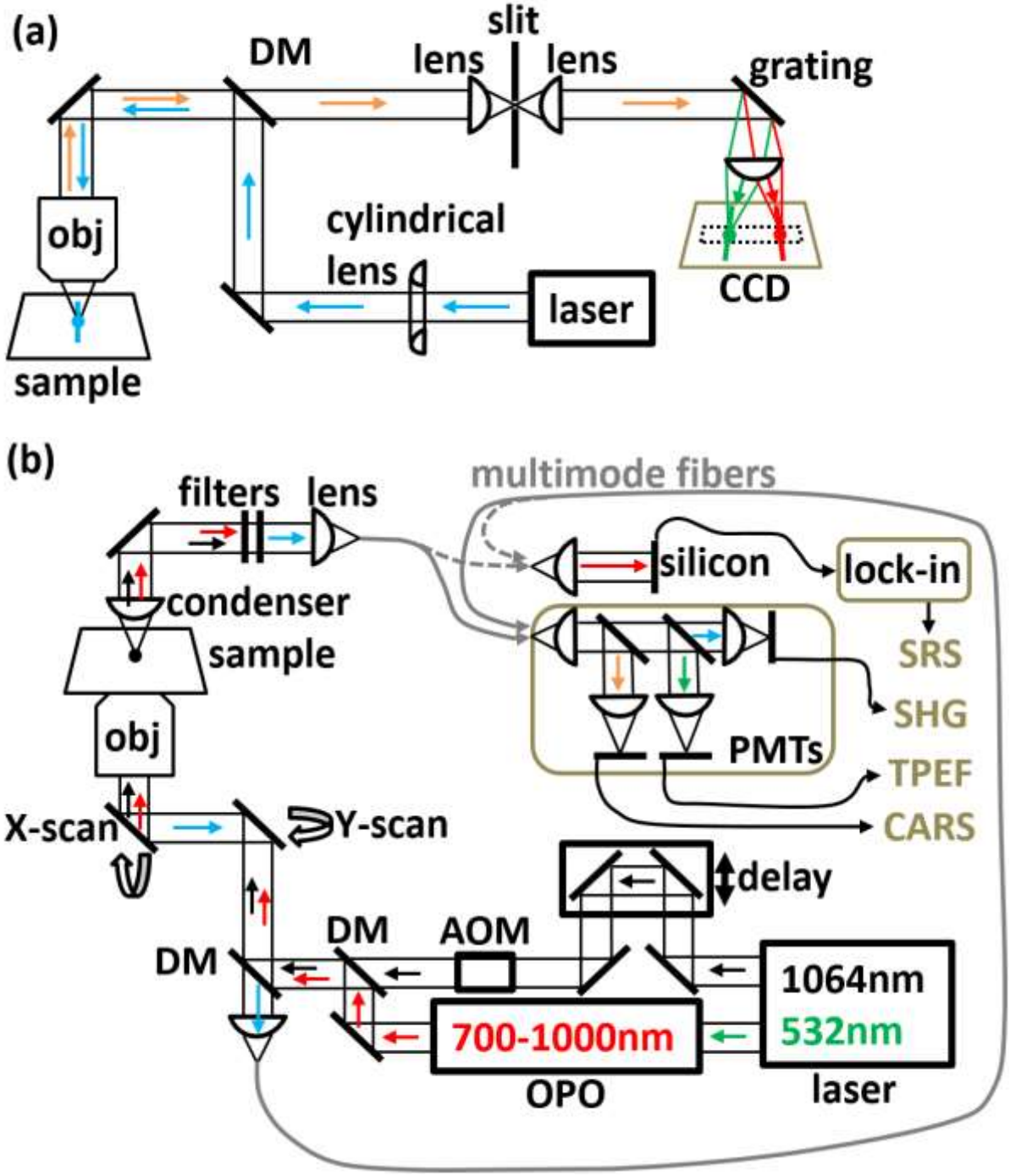


*Fig. 2. (a) Schematic of a confocal Raman spectrometer. In the first case, without a cylindrical lens present the Raman spectrum is acquired from the region of a diffraction-limited spot in the sample. This system acts as a confocal Raman microscope when the sample stage is raster-scanned and a spectrum acquired from each position. With a cylindrical lens present, a line-scanning Raman microscope is created. For line-scanning, effectively many separate focal spots are created along a line across the sample, with all the corresponding spectra recorded in parallel on the CCD detector. (b) Multi-photon microscope used for high speed Raman imaging – coherent anti-Stokes Raman scattering (CARS) microscopy and stimulated Raman scattering (SRS) microscopy, and complementary imaging techniques of two-photon excitation fluorescence (TPEF) and second harmonic generation (SHG). The laser produces picosecond pulses of one wavelength (in this case 1064 nm), and an optical parametric oscillator (OPO) provides a tuneable wavelength (700 - 1000 nm). These beams are combined so that*

*after passing through the objective lens (obj), they are both focussed at the same position on the sample, and are raster-scanned to produce an image. The frequency difference between the laser and OPO is chosen to match a vibrational frequency of interest. For modularity, signals are collected by multimode fibres and relayed to the detectors. In CARS, TPEF and SHG, high speed photomultiplier tube (PMT) detectors are used to acquire signals. In SRS microscopy, an acousto-optic modulator (AOM) 'chops' the intensity of laser light, and a lock-in amplifier records the modulation of the transmitted OPO light measured by a silicon photodiode.*

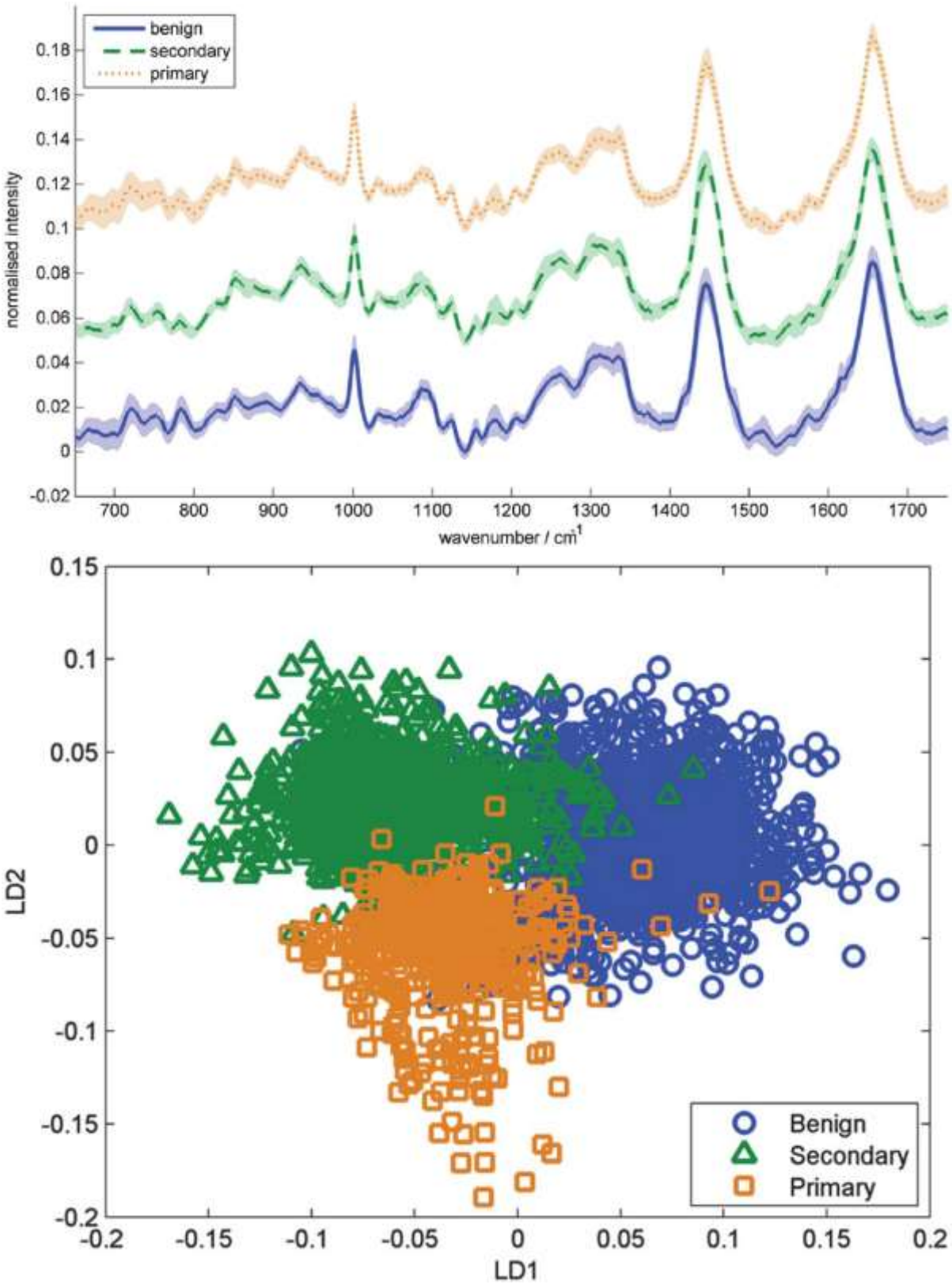


*Fig. 3. (Top:) Mean Raman spectra for each group of lymph nodes from the head and neck. Regions within frozen sections of lymph node tissue were assigned as primary tumor, secondary tumor, or healthy, by 3 pathologists investigating H&E stained sections. The shaded regions indicate +/- 1 standard deviation from the mean. (Bottom:) Linear discriminant analysis (LDA) plots for the three groups, using significant components from principal component analysis (PCA). Components which*

*showed a significant difference between the pathology groups at a 99% confidence level were used as the inputs to LDA (26).*

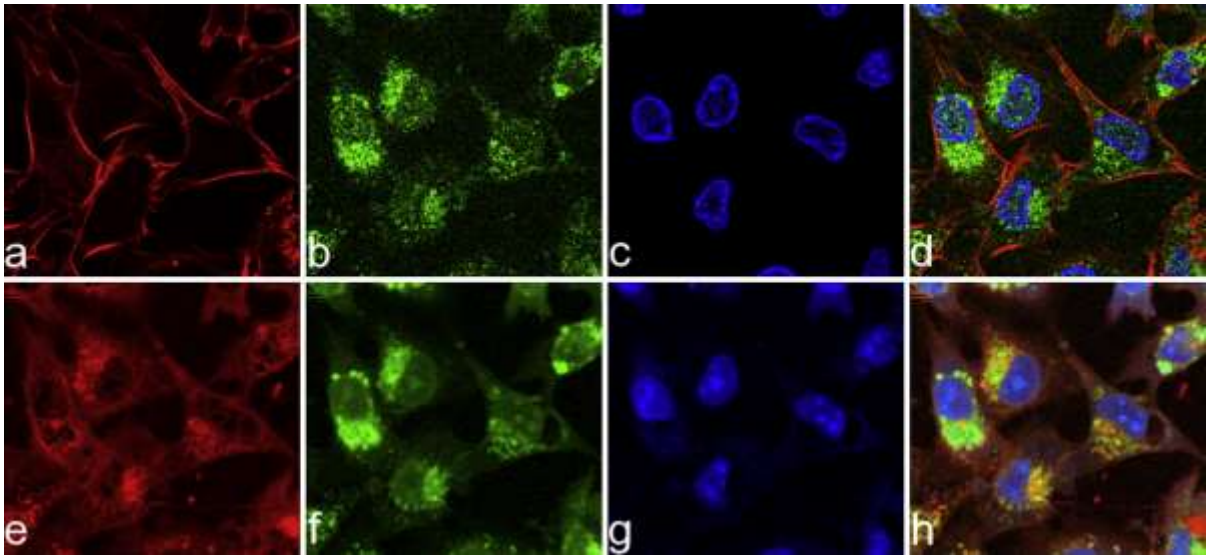


*Fig. 4. Comparison of fluorescently labelled cells (a–d) and label-free Raman microscopy (e–h) of organelles. Actin is highlighted in red in (a) and (e), Golgi apparatus is in green in (b) and (f), the nucleus is in blue in (c) and (g), and images are merged into (d) for fluorescence labelling, and (h) for label-free Raman microscopy (33).*

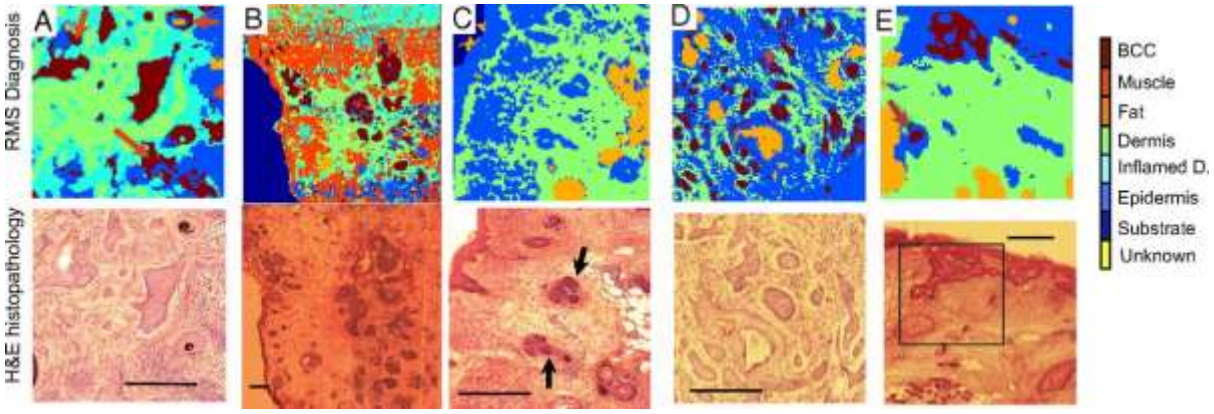


*Fig. 5. Diagnosis of basal cell carcinoma (BCC) by Raman microspectroscopy (RMS). Tissue sections: (A and B) nodular BCC; (C) BCC-negative skin sample containing hair follicles with morphology similar to that of BCC (black arrows). Unsectioned tissue layers: (D) infiltrative BCC; (E) superficial BCC. The histopathology images for adjacent sections are included for comparison. (Scale bars: 400 µm.) False positives are indicated by red arrows in (A). (42)*


*Fig. 6. Live SRS imaging of HeLa (cervical cancer) cells, incubated with 100 µM 5-ethynyl-2'-deoxyuridine (EdU), at three different frequencies. (Left:) The alkyne stretch frequency 2125 $cm^{-1}$, (centre:) a control image acquired at a frequency 2000 $cm^{-1}$ – well away from the alkyne vibration, (right:) amide frequency 1655 $cm^{-1}$ dominated by proteins. Together these images show that (i) alkyne-containing EdU is present only in the nucleus, and (ii) images have a very low background when not tuned to a particular vibrational bond. Scale bars, 10 µm (48).*

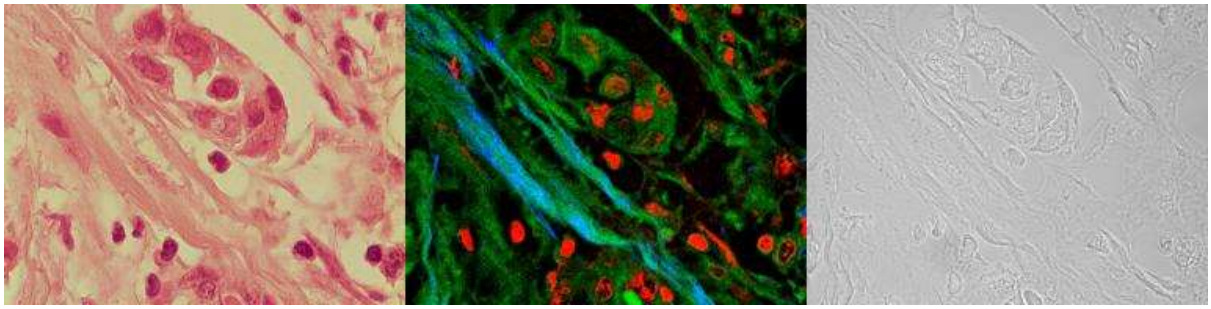

*Fig. 7. (Left:) Haematoxylin & eosin (H&E) stain of paraffin-embedded breast ductal carcinoma tissue section. Lipids and paraffin were removed by dewaxing in xylene. (Centre:) label-free multimodal image of an adjacent tissue section. CARS image obtained at the $CH_3$ vibration wavenumber (2930 $cm^{-1}$) in proteins (red) highlighting the solid tumors lying in a connective tissue composed of fibrous collagen and elastin probed with SHG (blue) and TPEF (green), respectively. The image acquisition time was 21 s per image, and image sizes are 100 × 75 µm. (Right:) transmitted light image of unstained tissue, of an adjacent section.*

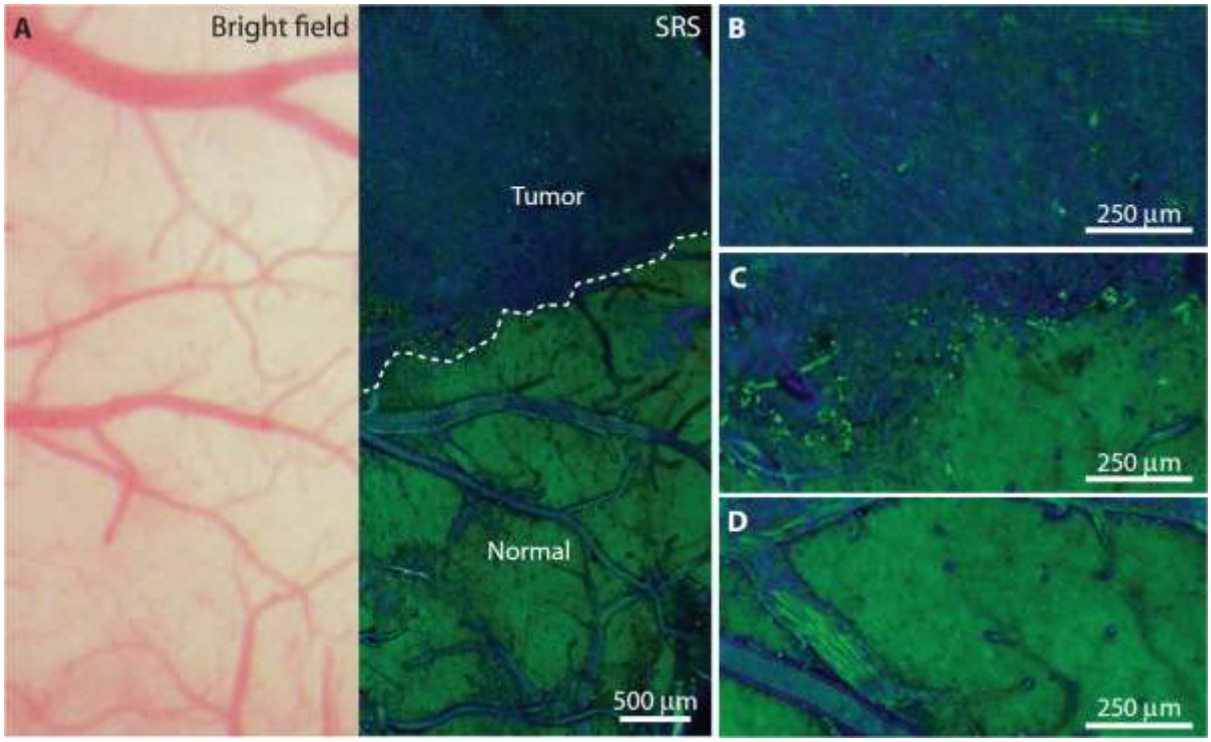


*Fig. 8. In vivo SRS microscopy images of human glioblastoma multiforme (GBM) xenografts. SRS imaging was carried out via acute cranial window preparation in mice 24 days after implantation of human GBM xenografts. (A) Bright-field microscopy appears grossly normal, whereas SRS microscopy within the same region demonstrates distinctions between tumor-infiltrated areas and non-infiltrated brain (normal), with a normal brain–tumor interface (dashed line). (B to D) High magnification views within the tumor (B), at the tumor-brain interface (C), and within normal brain (D). (57)*